VIP Drug Delivery Very Important Paper

DOI: 10.1002/ange.201311227

# Sequential Intra-Intercellular Nanoparticle Delivery System for Deep Tumor Penetration**

*Caoyun Ju, Ran Mo,* Jingwei Xue, Lei Zhang, Zekai Zhao, Lingjing Xue, Qineng Ping, and Can Zhang**

***Abstract:*** *To achieve deep tumor penetration of large-sized nanoparticles (NPs), we have developed a reversible swelling–shrinking nanogel in response to pH variation for a sequential intra-intercellular NP delivery. The nanogel had a crosslinked polyelectrolyte core, consisting of N-lysinal-N′-succinyl chitosan and poly(N-isopropylacrylamide), and a crosslinked bovine serum albumin shell, which was able to swell in an acidic environment and shrink back under neutral conditions. The swelling resulted in a rapid release of the encapsulated chemotherapeutics in the cancer cells for efficient cytotoxicity. After being liberated from the dead cells, the contractive nanogel could infect neighboring cancer cells closer to the center of the tumor tissue.*

Nanomedicine, typically a myriad of nanocarrier-based drug delivery systems (DDSs), provides emerging and promising opportunities to improve cancer therapy.[1] A number of nanoparticle (NP)-based therapeutics have been approved for clinical applications in solid tumors,[2] such as Doxil (pegylated liposomal doxorubicin, ca. 100 nm)[2c] and Abraxane (albumin-bound paclitaxel NP, ca. 130 nm).[2d–f] Despite of the improved therapeutic properties and reduced adverse effects owing to the enhanced permeability and retention (EPR) effect, it has been found that these NPs are predominantly located near the blood vessels and only delivered to the cells on the tumor periphery,[3] thus offering modest survival benefits,[4] which is primarily attributed to the physiological barriers of the solid tumor that impede the uniform distribution of the anticancer drugs throughout the tumor in a therapeutic concentration.[5]

The solid tumors are characterized by an abnormal tumor vasculature[6] and the dense tumor extracellular matrix (ECM).[7] High permeability of the abnormal tumor vasculature[6b,c] and lack of the lymphatic drainage system[6d] lead to a reduced transcapillary pressure gradient and an elevated interstitial fluid pressure (IFP),[8] which causes NPs to accumulate and release their payload only in the perivascular space of tumor areas, along with a higher drug efflux than influx into the tumor interstitium. Additionally, the denser fiber network of the connective tissue in the ECM promotes the build-up of a higher IFP and also leads to an increased frictional resistance to penetration. Of note, the hypoxic tumor cells in the center of the tumors harbor the stem cells, the most aggressive tumor cells, which can regenerate the tumor after therapy.[9] Unfortunately, the core of the solid tumors distant from the blood vessels is poorly perfused as a result of the above characteristics, which hinders the delivery of drugs to these tumor cells.

NPs with small particle sizes (< 100 nm) give a better tumor distribution than the larger ones.[10] For example, sub-100 nm polymeric micelles, especially 30 nm micelles, have been demonstrated to penetrate poorly permeable tumors to attain an optimal antitumor efficacy.[10c] Small-sized gold[10d,e] and silica[10f] NPs also displayed superior tumor penetration. To improve the tumor distribution and penetration of larger NPs, a multistage NP delivery system (QDGelNPs) has been reported to exhibit a deep penetration into the tumor tissue. The NP was composed of a gelatin core and a surface covered with quantum dots (QDs).[10g] When QDGelNPs (100 nm) accumulated at the tumor site, gelatinases A and B that are concentrated in the tumor environment hydrolyzed the gelatin core and thereby resulted in shedding of QDs (10 nm), which subsequently penetrated deep into the tumor. However, this system still depends on the tumor penetration capability of the ultra-small-sized QDs in fact. In addition, QDs cannot be applied as a carrier with high drug-loading efficiency alone. Accordingly, realization of the large NPs (> 100 nm) passing over the barriers of the solid tumor for deep penetration is very challenging but highly desirable.

Herein, we report a sequential intra-intercellular NP delivery of a reversible swelling-shrinking nanogel (NLSC-NG) as a novel mechanism for the large NPs to accomplish the deep tumor penetration. The nanogel has a well-defined core–shell crosslinked structure consisting of *N*-lysinal-*N*′-succinyl chitosan (NLSC), poly(*N*-isopropylacrylamide) (PNIPAM), and bovine serum albumin (BSA; Figure 1). NLSC is an optimized synthesized chitosan derivative with an

[*] Dr. C. Ju,[+] Dr. R. Mo,[+] J. Xue, L. Zhang, Z. Zhao, Dr. L. Xue, Prof. Q. Ping, Dr. C. Zhang
State Key Laboratory of Natural Medicines
Center of Drug Discovery and Department of Pharmaceutics
China Pharmaceutical University
24 Tong Jia Xiang, Nanjing, 210009 (China)
E-mail: rmocpu@gmail.com
zhangcan@cpu.edu.cn

[+] These authors contributed equally to this work.

[**] This work was supported by the National Natural Science Foundation of China (81072589, 81273468), State Key Laboratory of Natural Medicines at China Pharmaceutical University (SKLNMZZ201206, SKLNMZZCX201306), 111 Project from the Ministry of Education of China and the State Administration of Foreign Expert Affairs of China (No. 111-2-07) and the Fundamental Research Funds for the Central Universities (2410698). We greatly appreciated Prof. Gang Hu at Nanjing Medical University and Prof. Yong Yang at China Pharmaceutical University for valuable comments and suggestions. We also thank Prof. Gang Hu for providing us with the live cell imaging system.

Supporting information for this article is available on the WWW under http://dx.doi.org/10.1002/anie.201311227.

  

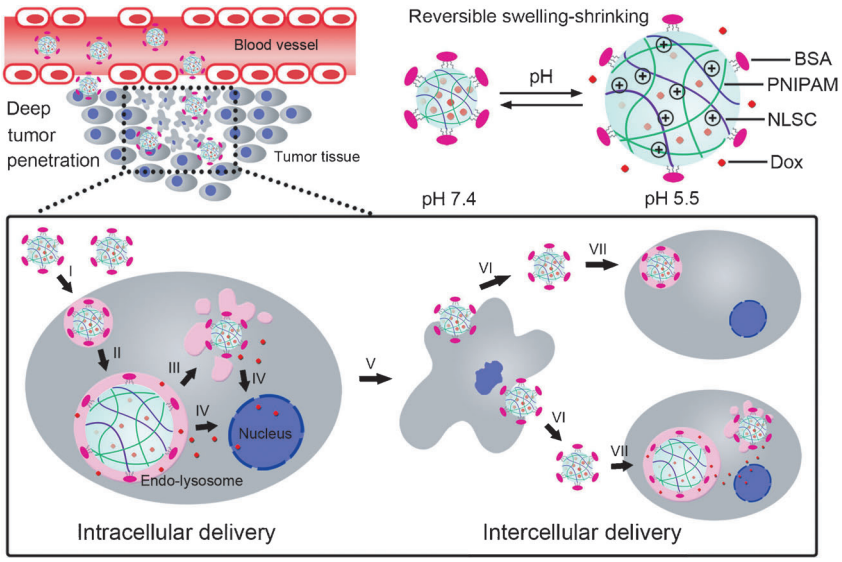


***Figure 1.*** Schematic design of the intra-intercellular NP delivery system based on a reversible swelling–shrinking nanogel (NLSC-NG) for deep tumor penetration. I) Endocytosis by the tumor cells after accumulation of Dox/NLSC-NG at the tumor site by the EPR effect; II) transport into endo-lysosomes; III) endo-lysosomal escape by the extensive volume expansion and high positive surface charge of Dox/NLSC-NG accompanied by the Dox release; IV) specific accumulation of the released Dox in the nucleus; V) cell death induced by the released Dox; VI) liberation from the dead cell; VII) migration and infection to the neighboring tumor cells.

isoelectric point (pI) around 6.0, which has an acid-triggered charge reversal capability. The polyelectrolyte core of the nanogel is constructed by polymerizing *N*-isopropylacrylamide (NIPAM) in the presence of NLSC under neutral conditions. BSA, a biocompatible negatively charged macromolecule, forms a capsid-like shell by crosslinking on the polyelectrolyte core, which retains the stability of the nanogel during the systemic circulation and the pH-responsive swelling–shrinking process. After intravenous administration, NLSC-NG which has a negative charge under physiological conditions (pH 7.4) accumulates at the tumor site by the EPR effect, and is subsequently internalized by the cells at the outer layer of the tumor tissue into the endosomes and lysosomes (endo-lysosomes). At the endosomal (pH 5.0–6.0) or lysosomal pH value (pH 4.0–5.0) which is lower than pI of NLSC, the amino groups in NLSC protonate promptly, which produces electrostatic repulsion between NLSC and therefore triggers the swelling of the polyelectrolyte core of NLSC-NG, along with the rapid release of the encapsulated anticancer drug, doxorubicin (Dox). The extensive volume expansion and positive surface charge of NLSC-NG lead to the endo-lysosomal bursting, which allows NLSC-NG to be transported into the cytosol (pH 6.8–7.4) where NLSC-NG rapidly shrinks back to its original size. The released Dox induces the apoptosis and cytotoxicity to kill the tumor cells. The contracted NLSC-NG is liberated from the dead cells potentially accompanied by exocytosis from the live cells to repeat the process infecting neighboring cancer cells closer to the center of the tumor. This sequential intra-intercellular NP delivery system, like "peeling an onion" layer by layer, offers an efficient nanocarrier platform with great potential for deep tumor penetration of anticancer drugs.

To validate our idea, NLSC was synthesized by grafting lysine and succinic anhydride to the backbone of chitosan (Figure S1, Supporting Information). The pI of NLSC was adjusted by changing the feeding ratio of lysinal and succinyl groups, and determined by measuring the optical transmittance of the NLSC solution at different pH values (Figure S2). NLSC with pI of 6.0 was selected to have the optimal pH-sensitivity, undergoing charge conversion at the acidity of endo-lysosome (pH 4.0–6.0) in contrast to NLC which has a positive charge regardless of pH values. The substitution degrees of lysinal and succinyl groups were 43% and 66%, respectively (Table S1).

The core–shell NLSC-NG was then successfully fabricated by chemically conjugating the BSA shell onto the polyelectrolyte core consisting of PNIPAM and NLSC. The

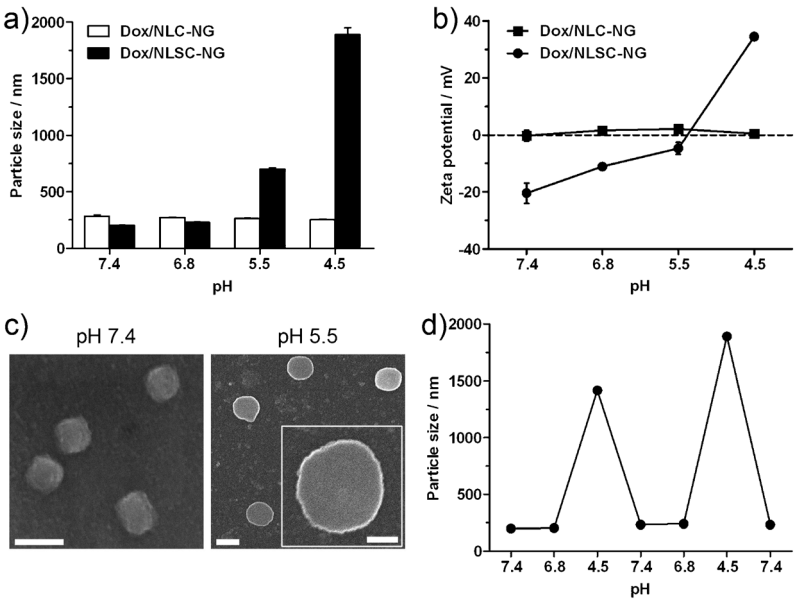


***Figure 2.*** a) Particle size of Dox/NLC-NG and Dox/NLSC-NG at different pH values. b) Zeta potential of Dox/NLC-NG and Dox/NLSC-NG at different pH values. c) FESEM images of Dox/NLSC-NG at pH 7.4 and 5.5. Scale bars are 200 nm (left), 500 nm (middle), and 200 nm (right). d) Change in the particle size of Dox/NLSC-NG with pH value.

content of BSA conjugated on NLSC-NG was about 88 μg for 1 mg of NLSC-NG. The pH-sensitivity of NLSC-NG was assessed by monitoring the optical transmittance change with pH value (Figure S3). The transmittance percentage changed sharply over the pH range of 6.6–5.5, which resulted from the dynamic dimensional variations of NLSC-NG with pH value. Dox, a model chemotherapeutic agent, was efficiently physically encapsulated in NLSC-NG. The payload of Dox in NLSC-NG was high, up to 27%, while NLC-NG had a lower drug-loading efficiency of about 5%, suggesting that the electrostatic interaction between the negatively charged NLSC at neutral pH values and the positively charged Dox molecules facilitates the encapsulation of Dox into the polyelectrolyte core of NLSC-NG.

To demonstrate the acid-responsive swelling of NLSC-NG, we measured the particle size and zeta potential of Dox-loaded NLSC-NG (Dox/NLSC-NG) dispersed in buffer solutions with different pH values. Note that all the measurements were at 37°C, higher than the low critical solution temperature (LCST) of NLSC-NG (about 32°C; Figure S4), which indicated that the presence of PNIPAM had no influence on the pH-sensitivity of the nanogel at 37°C. When the pH decreased from 7.4 to 4.5 (the typical lysosomal pH value), Dox/NLSC-NG increased in particle size from 200 nm at pH 7.4 to near 2 μm at pH 4.5 (Figure 2a and Table S2), and showed a change in the surface charge from −20 mV at pH 7.4 to +35 mV at pH 4.5 (Figure 2b). The field emission scanning electron microscope (FESEM; Figure 2c and Figure S5), transmission electron microscope (Figure S6), and atomic force microscope (AFM) (Figure S7) images further demonstrated the volumetric increase of Dox/NLSC-NG at pH 5.5 or 4.5 relative to pH 7.4. In sharp contrast, no volume swelling and surface charge conversion were found in Dox-loaded NLC-NG (Dox/NLC-NG) during such a pH change. The percentage of protonated amino groups in NLSC-NG at different pH values was determined to be about 9.5% at pH 7.4, 29.4% at pH 6.8, 89.3% at pH 5.5, and 98.8% at pH 4.5 (Figure S8). It was speculated that the prompt protonation of the amino groups in NLSC-NG produces the electrostatic repulsion between NLSC under acidic conditions, causing the swelling of the polyelectrolyte core, and thus the particle size increase of NLSC-NG. The extensive volume expansion and electrostatic repulsion between the positively charged core and Dox at lower pH values contributed to the increased release of Dox from Dox/NLSC-NG (Figure S9).

We further evaluated the pH-responsive reversible swelling–shrinking property of NLSC-NG (Figure 2d and Table S3). Dox/NLSC-NG showed a reversible swelling and shrinking when the pH value was cycled from 7.4 to 6.8 to 4.5. The particle size was constant about 200 nm from pH 7.4 to 6.8 (the typical tumor extracellular and cytosolic pH values), sharply increased by 10-fold at pH 4.5, and then returned to 240 nm at pH 6.8. Apparently, the structure of NLSC-NG remains stable owing to the BSA shell that clutches the inner polyelectrolyte core by means of amide linkages, which avoids the dissociation after protonation of the core at lower pH values. The BSA shell also maintained the stability of Dox/NLSC-NG in the presence of plasma (Figure S10).

The intra-intercellular delivery of Dox/NLSC-NG was evaluated in/among the human hepatocellular carcinoma (HepG2) cells. Both Dox/NLSC-NG and Dox/NLC-NG were

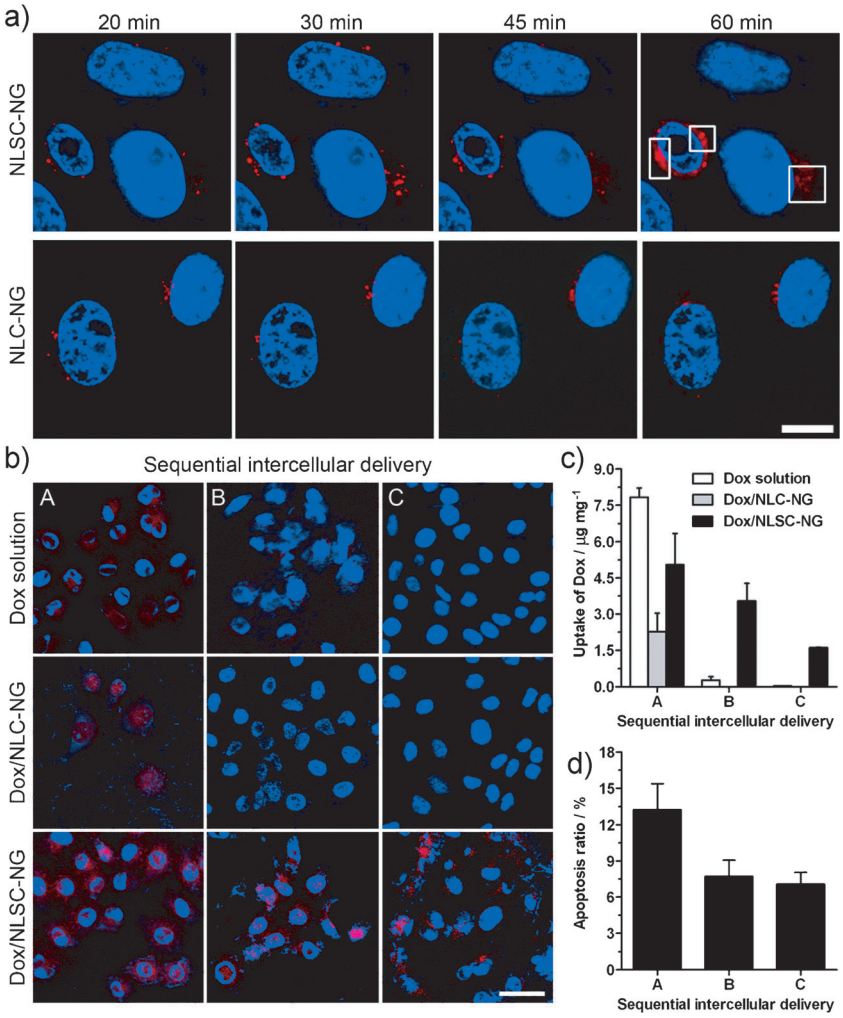


***Figure 3.*** a) Endo-lysosomal appearance of the live HepG2 cells incubated with NLSC-NG and NLC-NG over time observed using the live cell imaging. The late endosomes and lysosomes were stained by LysoTracker Red. The squares indicate the bursting of endo-lysosomes. Scale bar is 10 μm. b) Migration of Dox/NLSC-NG from the infected HepG2 cells to the untreated cells visualized using CLSM (see text for details). The Dox solution and Dox/NLC-NG were taken as references. The nuclei were stained by Hoechst 33258. Scale bar is 20 μm. c) Cellular uptake of Dox in the infected HepG2 cells. d) Apoptosis ratio of the infected HepG2 cells induced by Dox/NLSC-NG using the Annexin V-FITC/PI staining assay.

internalized through the clathrin-mediated endocytosis pathway (Figure S11), and subsequent localization in the endosomes.[11] To verify the endo-lysosomal bursting effect of NLSC-NG upon the pH-responsive swelling, fluorescence-labeled endo-lysosomes of HepG2 cells incubated with the bare NLSC-NG over time were monitored by the live cell imaging (Figure 3a). After cell incubation with NLSC-NG for 60 min, the dot-like appearance of the endo-lysosomes disappeared, and an originally localized "burst" of fluorescence diffusion was observed instead. In contrast, no significant change in the endo-lysosomal aspect was found during treatment with NLC-NG. The prominent expansion and high positive surface charge of NLSC-NG were determined to promote the disruption of endo-lysosomal membranes (Figure S12), which allows NLSC-NG to translocate from the endo-lysosomes to the cytosol where NLSC-NG rapidly shrinks back to the initial size. Additionally, the AFM images showed that NLSC-NG was still able to swell and shrink with pH change after transport from HepG2 cells (Figure S13). It was suggested that NLSC-NG retains its pH-responsive reversible swelling–shrinking capacity even after the intracellular delivery, which lays a good foundation for subsequent intercellular delivery.

To explore the intercellular delivery of NLSC-NG to the neighboring cells, HepG2 cells seeded on Coverslip A were pre-incubated with Dox/NLSC-NG for 8 h, and then co-incubated with the fresh cells on the neighboring Coverslip B for 20 h. The infection procedure was repeated by co-incubating the treated cells on Coverslip B with the fresh cells on Coverslip C for another 20 h, followed by observation using confocal laser scanning microscope (CLSM). As shown in Figure 3b, the red Dox fluorescence in the first treated cells (A) with Dox/NLSC-NG indicated that Dox widely distributed in the cells, even in the blue fluorescent nuclei. After successive co-incubation with the untreated cells for 20 h, the infected cells (B) showed the Dox fluorescence in the nuclei as well, and additionally, the Dox fluorescence was still observed in the infected cells (C). However, free Dox and Dox/NLC-NG hardly attained the Dox fluorescence in the cells (B, C), indicating that they have no repeated infection properties. Quantitative analysis substantiated that Dox/NLSC-NG provided significantly higher Dox accumulation in the infected cells than either the Dox solution or Dox/NLC-NG (Figure 3c). The amounts of Dox released from the infected cells treated by Dox/NLSC-NG was much higher than that treated by Dox/NLC-NG (Figure S14a), most of which was encapsulated in the exocytosed NLSC-NG for repeated infection (Figure S14b). Furthermore, we confirmed that Dox/NLSC-NG was able to induce apoptosis of the infected cells during the intercellular trafficking (Figure 3d). Taken together, Dox/NLSC-NG like a virus is able to release Dox in the infected cells to induce cell death, transport from the dead cells potentially along with exocytosis from the live cells, and infect the neighboring cells.

To further verify the enhanced tumor penetration of drugs by this intra-intercellular delivery mechanism, the multicellular tumor spheroids, three-dimensional (3D) cell culture systems were first used to monitor the penetration of Dox/NLSC-NG in an in vivo-like tumor (Figure 4a). After the tumor spheroid treated with Dox/NLSC-NG for 8 h, Dox with the bright red fluorescence spread in the majority of regions, even 80 μm from the surface towards the middle. It was determined to penetrate approximately 27% of the tumor spheroid which has a radius of about 300 μm. By comparison, the tumor spheroids treated with Dox/NLC-NG only showed a Dox fluorescence distribution at the periphery of the spheroids. Moreover, a multitude of cell fragments were shed from the surface of the tumor spheriods after treatment with Dox/NLSC-NG, which might result from the apoptosis induced by Dox/NLSC-NG, while no remarkable change was observed in the morphology of the Dox/NLC-NG treated tumor spheriods. After intravenous injection into the hepatocellular carcinoma (Heps) tumor-bearing mice for 48 h, Dox/NLSC-NG rather than Dox/NLC-NG facilitated the

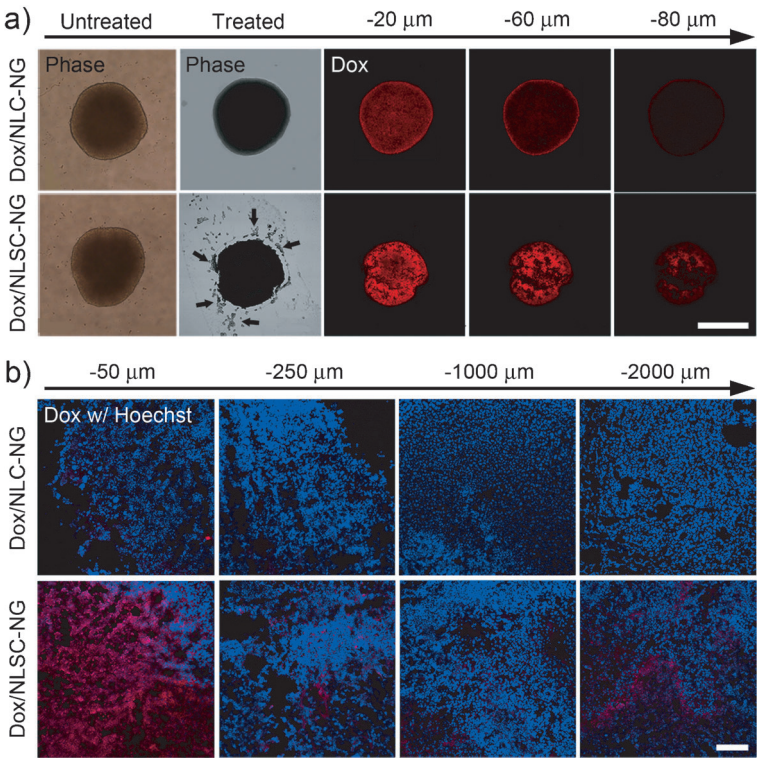


***Figure 4.*** a) In vitro penetration of Dox into the 3D multicellular HepG2 tumor spheroids after incubation with Dox/NLC-NG and Dox/NLSC-NG for 8 h. Z-stack images using CLSM were obtained from the top to the equatorial plane of the tumor spheroid in 20 μm thickness. The arrows indicate the cell fragments shedding from the surface of the tumor spheroids. Scale bar is 400 μm. b) In vivo penetration of Dox into the tumors of the Heps tumor-bearing mice after intratumoral injection of Dox/NLC-NG and Dox/NLSC-NG at Dox dosage of 10 mg kg$^{-1}$ for 48 h. The frozen tumor sections were observed at different depths below the injection site using CLSM. The nuclei were stained by Hoechst. Scale bar is 200 μm.

extravasation of Dox outside of the tumor vasculature and the penetration of Dox in the surrounding tumor tissue (Figure S15). Furthermore, Dox/NLSC-NG were injected intratumorally at a fixed depth of needle insertion into the Heps tumor-bearing mice to confirm the deep tumor penetration effect of NLSC-NG (Figure 4b).[10g] At 48 h post-injection of Dox/NLSC-NG, Dox distributed evenly in each tumor section, even at 2000 μm inside the tumor below the injection site, while only very weak Dox fluorescence could be observed after applying Dox/NLC-NG at the depth range of 50 to 250 μm. Collectively, NLSC-NG was able to efficiently deliver the drug cargo from the exterior to the interior of the solid tumor.

The in vitro cytotoxicity of Dox/NLSC-NG against HepG2 cells was estimated using the 3-(4,5-dimethylthiazol-2-yl)-2,5-diphenyltetrazolium bromide (MTT) assay (Figure 5a,b). Dox/NLC-NG had a lower cytotoxicity toward HepG2 cells. The viability of the cells was about 68%, even at Dox concentration of 10 $\mu g\,mL^{-1}$ for 48 h treatment. In contrast, Dox/NLSC-NG showed significantly enhanced cytotoxicity as incubation time increased. The half-maximal inhibitory concentration of Dox/NLSC-NG was about 2.6 $\mu g\,mL^{-1}$ for 24 h and 0.49 $\mu g\,mL^{-1}$ for 48 h, which indicated a fourfold increase in the cytotoxicity. When the incubation time extended to 72 h, Dox/NLSC-NG presented a comparable cytotoxicity to the Dox solution, which had an inhibition ratio of 80% even at Dox concentration of 100 $ng\,mL^{-1}$ (Figure S16). The bare nanogels without Dox did not show toxicity at any of the studied concentrations (Figure S17).

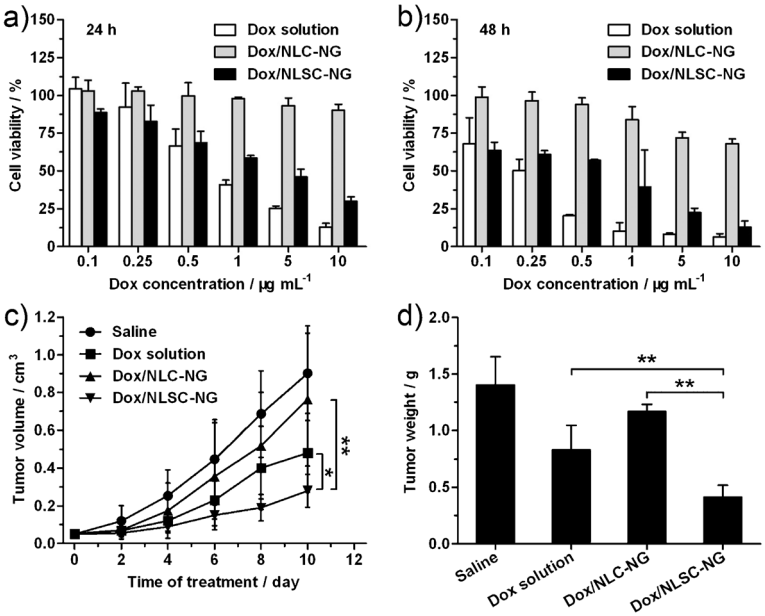


***Figure 5.*** a,b) In vitro cytotoxicity of the Dox solution, Dox/NLC-NG and Dox/NLSC-NG on HepG2 cells for 24 h (a) and 48 h (b). c) Tumor growth curves of the Heps tumor-bearing mice following intravenous injection of the Dox solution, Dox/NLC-NG and Dox/NLSC-NG at Dox dosage of 10 $mg\,kg^{-1}$. $*P<0.05$, $**P<0.01$. d) Tumor weights of the Heps tumor-bearing mice after the treatment at day 10. $**P<0.01$.

The antitumor activity of Dox/NLSC-NG was further evaluated using Heps tumor xenograft models. Dox/NLSC-NG showed greater blood persistence than the Dox solution (Figure S18 and Table S4). Such a significant difference suggested that Dox/NLSC-NG can maintain a high concentration of Dox in the blood for a longer time. As expected, Dox/NLSC-NG showed a prominent effect on inhibiting tumor growth compared with the Dox solution and Dox/NLC-NG (Figure 5c). The tumor growth inhibition rate of Dox/NLSC-NG was about 70% compared with 39% of the Dox solution and 17% of Dox/NLC-NG (Figure 5d). Insignificant difference in the body weights of the mice was found during the treatment of Dox/NLSC-NG compared with saline (Figure S19). The histologic sections stained by hematoxylin and eosin displayed that the treatment of Dox/NLSC-NG resulted in a large region of cancer cell remission in the tumor tissue (Figure S20) but no apparent toxic effects in the heart (Figure S21), such as cardiomyopathy mainly observed in Dox cancer treatment.[12]

In summary, we have developed a new virus-like pH-responsive intra-intercellular NP delivery system, which was composed of all-biopolymer-based nanogels with a polyelectrolyte core and a crosslinked protein shell. The obtained nanogels presented pH-sensitive reversible swelling–shrinking capability, which was able to repeatedly infect the neighboring cells accompanied by the on-demand intracellular release of anticancer drug to induce the cell death. Based on this intra-intercellular delivery mechanism, the nanogels helped the drugs penetrate deep into the solid tumor for enhanced therapeutic efficacy. We believe that this strategy will provide opportunities to explore more intelligent drug delivery nanoplatforms for deep tumor penetration in future.

Received: December 27, 2013
Published online: April 16, 2014

**Keywords:** antitumor agents · drug delivery · nanogels · pH responsive · tumor penetration

[1] a) D. Peer, J. M. Karp, S. Hong, O. C. Faro Khzad, R. Margalit, R. Langer, *Nat. Nanotechnol.* **2007**, *2*, 751–760; b) R. K. Jain, T. Stylianopoulos, *Nat. Rev. Clin. Oncol.* **2010**, *7*, 653–664; c) H. Cabral, N. Nishiyama, K. Kataoka, *Acc. Chem. Res.* **2011**, *44*, 999–1008; d) R. Mo, T. Jiang, R. DiSanto, W. Tai, Z. Gu, *Nat. Commun.* **2014**, *5*, 3364.

[2] a) L. Zhang, F. X. Gu, J. M. Chan, A. Z. Wang, R. S. Langer, O. C. Farokhzad, *Clin. Pharmacol. Ther.* **2008**, *83*, 761–769; b) R. D. Hofheinz, S. U. Gnad-Vogt, U. Beyer, A. Hochhaus, *Anticancer Drugs* **2005**, *16*, 691–707; c) Y. Barenholz, *J. Controlled Release* **2012**, *160*, 117–134; d) K. Altundag, D. S. Dede, T. Purnak, *J. Clin. Pathol.* **2007**, *60*, 958–958; e) E. Miele, G. P. Spinelli, E. Miele, F. Tomao, S. Tomao, *Int. J. Nanomed.* **2009**, *4*, 99–105; f) L. Zhang, P. Marrano, S. Kumar, M. Leadley, E. Elias, P. S. Thorner, S. Baruchel, *Clin. Cancer Res.* **2013**, *19*, 5972–5983.

[3] a) F. Yuan, M. Leunig, S. K. Huang, D. A. Berk, D. Papahadjopoulos, R. K. Jain, *Cancer Res.* **1994**, *54*, 3352–3356; b) Y.

  

Tsukioka, Y. Matsumura, T. Hamaguchi, H. Koike, F. Moriyasu, T. Kakizoe, *Jpn. J. Cancer Res.* **2002**, *93*, 1145 – 1153; c) R. B. Campbell, D. Fukumura, E. B. Brown, L. M. Mazzola, Y. Izumi, R. K. Jain, V. P. Torchilin, L. L. Munn, *Cancer Res.* **2002**, *62*, 6831 – 6836.

[4] a) E. P. Winer, D. A. Berry, S. Woolf, W. Duggan, A. Kornblith, L. N. Harris, R. A. Michaelson, J. A. Kirshner, G. F. Fleming, M. C. Perry, M. L. Graham, S. A. Sharp, R. Keresztes, C. I. Henderson, C. Hudis, H. Muss, L. Norton, *J. Clin. Oncol.* **2004**, *22*, 2061 – 2068; b) M. E. O'Brien, N. Wigler, M. Inbar, R. Rosso, E. Grischke, A. Santoro, R. Catane, D. G. Kieback, P. Tomczak, S. P. Ackland, F. Orlandi, L. Mellars, L. Alland, C. Tendler, *Ann. Oncol.* **2004**, *15*, 440 – 449; c) W. J. Gradishar, S. Tjulandin, N. Davidson, H. Shaw, N. Desai, P. Bhar, M. Hawkins, J. O'Shaughnessy, *J. Clin. Oncol.* **2005**, *23*, 7794 – 7803.

[5] a) R. K. Jain, *Adv. Drug Delivery Rev.* **2001**, *46*, 149 – 168; b) R. K. Jain, *Sci. Am.* **2008**, *298*, 56 – 63; c) See Ref. [1b].

[6] a) R. K. Jain, *Cancer Res.* **1988**, *48*, 2641 – 2658; b) P. Carmeliet, R. K. Jain, *Nature* **2000**, *407*, 249 – 257; c) H. Hashizume, P. Baluk, S. Morikawa, J. W. McLean, G. Thurston, S. Roberge, R. K. Jain, D. M. McDonald, *Am. J. Pathol.* **2000**, *156*, 1363 – 1380; d) A. J. Leu, D. A. Berk, A. Lymboussaki, K. Alitalo, R. K. Jain, *Cancer Res.* **2000**, *60*, 4324 – 4327.

[7] a) P. A. Netti, D. A. Berk, M. A. Swartz, A. J. Grodzinsky, R. K. Jain, *Cancer Res.* **2000**, *60*, 2497 – 2503; b) N. E. Campbell, L. Kellenberger, J. Greenaway, R. A. Moorehead, N. M. Linnerth-Petrik, J. Petrik, *J. Oncol.* **2010**, 586905; c) P. F. Lu, V. M. Weaver, Z. Werb, *J. Cell Biol.* **2012**, *196*, 395 – 406.

[8] a) C. H. Heldin, K. Rubin, K. Pietras, A. Ostman, *Nat. Rev. Cancer* **2004**, *4*, 806 – 813; b) T. G. Simonsen, J. V. Gaustad, M. N. Leinaas, E. K. Rofstad, *PLoS One* **2012**, *7*, e40006.

[9] a) M. Dean, T. Fojo, S. Bates, *Nat. Rev. Cancer* **2005**, *5*, 275 – 284; b) J. E. Visvader, G. J. Lindeman, *Nat. Rev. Cancer* **2008**, *8*, 755 – 768; c) P. C. Hermann, S. Bhaskar, M. Cioffi, C. Heeschen, *Semin. Cancer Biol.* **2010**, *20*, 77 – 84.

[10] a) K. Kostarelos, D. Emfietzoglou, A. Papakostas, W. H. Yang, A. M. Ballangrud, G. Sgouros, *J. Liposome Res.* **2005**, *15*, 15 – 27; b) N. Tang, G. Du, N. Wang, C. Liu, H. Hang, W. Liang, *J. Natl. Cancer Inst.* **2007**, *99*, 1004 – 1015; c) H. Cabral, Y. Matsumoto, K. Mizuno, Q. Chen, M. Murakami, M. Kimura, Y. Terada, M. R. Kano, K. Miyazono, M. Uesaka, N. Nishiyama, K. Kataoka, *Nat. Nanotechnol.* **2011**, *6*, 815 – 823; d) K. Huang, H. Ma, J. Liu, S. Huo, A. Kumar, T. Wei, X. Zhang, S. Jin, Y. Gan, P. C. Wang, S. He, X. J. Liang, *ACS Nano* **2012**, *6*, 4483 – 4493; e) S. Huo, H. Ma, K. Huang, J. Liu, T. Wei, S. Jin, J. Zhang, S. He, X. J. Liang, *Cancer Res.* **2013**, *73*, 319 – 330; f) L. Tang, N. P. Gabrielson, F. M. Uckun, T. M. Fan, J. Cheng, *Mol. Pharm.* **2013**, *10*, 883 – 892; g) C. Wong, T. Stylianopoulos, J. Cui, J. Martin, V. P. Chauhan, W. Jiang, Z. Popović, R. K. Jain, M. G. Bawendi, D. Fukumura, *Proc. Natl. Acad. Sci. USA* **2011**, *108*, 2426 – 2431; h) R. Tong, H. H. Chiang, D. S. Kohane, *Proc. Natl. Acad. Sci. USA* **2013**, *110*, 19048 – 19053.

[11] a) G. J. Doherty, H. T. McMahon, *Annu. Rev. Biochem.* **2009**, *78*, 857 – 902; b) E. S. Lee, D. Kim, Y. S. Youn, K. T. Oh, Y. H. Bae, *Angew. Chem.* **2008**, *120*, 2452 – 2455; *Angew. Chem. Int. Ed.* **2008**, *47*, 2418 – 2421; c) R. Mo, Q. Sun, J. Xue, N. Li, W. Li, C. Zhang, Q. Ping, *Adv. Mater.* **2012**, *24*, 3659 – 3665.

[12] a) G. Takemura, H. Fujiwara, *Prog. Cardiovasc. Dis.* **2007**, *49*, 330 – 352; b) T. Safra, F. Muggia, S. Jeffers, D. Tsao-Wei, S. Groshen, O. Lyass, R. Henderson, G. Berry, A. Gabizon, *Ann. Oncol.* **2000**, *11*, 1029 – 1033; c) P. K. Singal, N. Iliskovic, *N. Engl. J. Med.* **1998**, *339*, 900 – 905.